ISSN (Print) 1226-1750
ISSN (Online) 2233-6656
Journal of Magnetics 30(4), 781-793 (2025) https://doi.org/10.4283/JMAG.2025.30.4.781

An Automated Electrode Placement Method for Optimizing Non-Invasive Electromagnetic Brain Stimulation

Min Joo Woo[1], Ga Yeon Park[1], Tae-Gyu Kim[2], Garam Lee[3], Won Kee Chang[4], Nam-Jong Paik[4]*, and Young-Jin Jung[1,2]*

[1]School of Healthcare and Biomedical Engineering, Chonnam National University, Yeosu 59626, Republic of Korea
[2]Dept. of Biomedical Engineering, Chonnam National University, Yeosu 59626, Republic of Korea
[3]Department of Health Science and Technology, Seoul National University, Seoul 08826, Republic of Korea
[4]Department of Rehabilitation Medicine, Seoul National University Bundang Hospital, Seoul 13620, Republic of Korea

(Received 5 November 2025, Received in final form 12 December 2025, Accepted 15 December 2025)

Transcranial electrical stimulation techniques such as transcranial direct current stimulation (tDCS), transcranial alternating current stimulation (tACS), and temporal interference stimulation (TIS) require accurate and reproducible electrode placement to achieve precise electric field targeting. However, conventional electroencephalography (EEG) electrode placement systems (10–20 and 10–10) cover only the scalp and are limited in stimulating cerebellar or deep brain regions. In this study, we developed an extended EEG-based electrode localization algorithm that includes both facial and lower occipital regions on a 3D human head mesh model. The algorithm, implemented in MATLAB, uses four anatomical landmarks to automatically compute 3D electrode coordinates and introduces new chin and posterior (inferior occipital) reference points to expand coverage. The proposed method minimizes spatial placement error and provides a standardized, visualizable framework for high-precision electromagnetic stimulation in research and clinical applications.

Keywords : Cerebellum stimulation, electromagnetic stimulation, EEG coordinate system, transcranial current stimulation, temporal interference stimulation (TIS)

1. Introduction

Recently, various non-invasive electromagnetic brain stimulation techniques, including transcranial direct current stimulation (tDCS), transcranial alternating current stimulation (tACS), and temporal interference stimulation (TIS), have been actively investigated [1–3]. To ensure the reliability and reproducibility of these studies, electrode placements based on standard EEG (electroencephalography) coordinate systems are commonly used [4–6]. However, the international 10–20 and 10–10 EEG placement systems were primarily developed for scalp electrodes and have important limitations: they do not adequately cover facial or lower occipital regions, which are required to stimulate deep brain structures such as the hippocampus, brainstem, or cerebellum. In practice, delivering current to deep targets with scalp-only electrodes is difficult unless very high currents are used, which can cause excessive cortical stimulation and safety issues [7–9].

To overcome these depth-targeting limitations, Grossman *et al.* introduced the TIS technique. TIS uses multiple pairs of electrodes driving high-frequency alternating currents that interfere within the brain, producing a low-frequency envelope of electric field only at the desired deep target [3]. A key feature of TIS is that it requires carefully positioning multiple electrode pairs across the scalp to direct the interference pattern. The distances and relative placement of these electrodes are critical for focusing the stimulation at the target region. In recent experimental studies, new electrode montages have been explored. For example, in recent human TIS trials targeting the hippocampus, researchers placed one electrode pair on the face (near the nasal bridge) and another above the eyebrow. Similarly, cerebellar tDCS often uses an electrode over the cerebellar region at the back of the head and a return electrode on the cheek (buccinator muscle). It has been reported that placing an electrode on the cheek, as opposed to only on the scalp,

*Corresponding author: Tel: +82-61-659-7366
Fax: +82-61-659-7369, e-mail: yj@jnu.ac.kr
e-mail: njpaik@snu.ac.kr

alters the current distribution reaching the cerebellum and can affect stimulation outcomes, leading some clinical studies to adopt cheek electrode placements. These examples illustrate a growing trend to extend EEG electrode placement techniques beyond the traditional scalp coverage in order to support emerging stimulation paradigms.

In summary, optimal electrode montages for deep or lower-brain targets require moving beyond the standard EEG cap placements. Non-invasive electromagnetic stimulation of deep brain areas necessitates an approach that expands electrodes onto the face and lower occipital regions. However, accurately and consistently positioning electrodes on the face or inferior head is challenging. Traditional manual measurement methods using EEG caps or tape measures can introduce large inter-operator errors and poor reproducibility, especially given individual variability in head shape. In brain stimulation research, a mismatch between the planned (simulated) target location and the actual electrode placement can significantly reduce the efficacy of the stimulation, so a precise electrode positioning technique is essential. In response to this need, recent efforts have turned to computational algorithms and digital tools to assist with electrode location planning.

As a representative prior work, Giacometti *et al.* developed an algorithm (sometimes referred to as the "Mesh2EEG" tool) that automatically computes electrode coordinates for the 10–20, 10–10, and even 10–5 systems on a 3D head surface mesh [5]. This method uses user-identified cranial landmarks (the nasion, inion, and left/right preauricular points) to define intersecting planes on the mesh, computes evenly spaced points along the head surface, and iteratively finds the coordinates of all standard electrode positions. By using such an approach, standard EEG electrode locations can be mapped onto an individual's head model obtained from MRI or CT scans without manual measurement, yielding accurate coordinates automatically. However, the Mesh2EEG approach has limitations in that it still focuses on the traditional head region: it can compute positions up to the 10–5 system on the scalp, but it does not provide coordinates outside the usual scalp boundary (for example, on the cheeks or lower back of the head). In other words, it does not support placing electrodes on facial areas or below the hairline (such as under the forehead or behind the ears).

To address these gaps, in this study we developed a new electrode placement algorithm that extends the standard EEG coordinate system to include the face and cerebellar (lower occipital) regions. The algorithm automatically computes and visualizes electrode locations on a 3D human head model within a MATLAB environment. Our approach is designed to minimize variability caused by electrode placement errors and to improve placement precision in both research and clinical trials that utilize the EEG coordinate framework. In the following, we present the implementation of this algorithm and demonstrate its results. Ultimately, by sharing the algorithm and software with the community, we aim to contribute to more precise and reproducible electrode placement for high-precision non-invasive brain stimulation.

2. Methods

The proposed method computes standard EEG electrode coordinates and then extends the placement to additional facial and cerebellar positions on a 3D head mesh. The algorithm takes as input a 3D surface mesh of the human

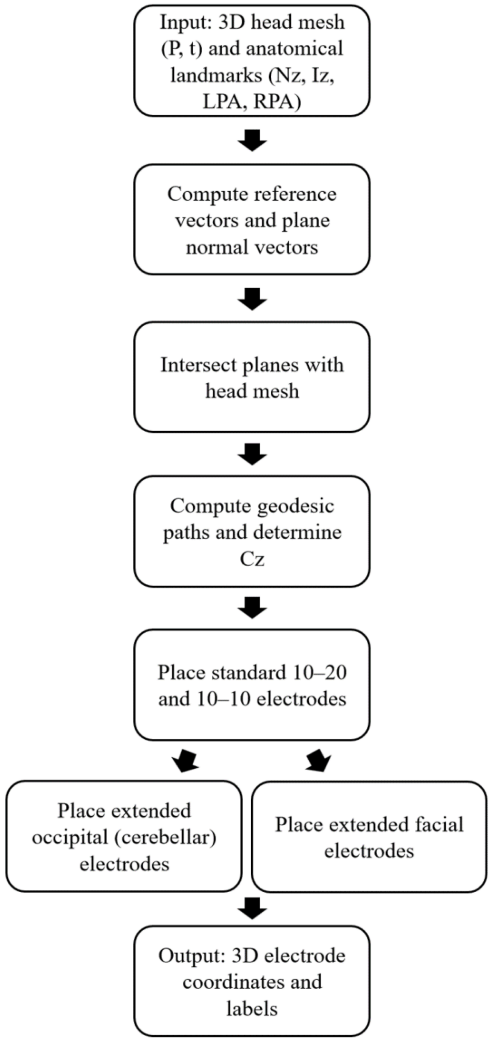

Fig. 1. Flowchart of the proposed EEG electrode localization algorithm.

head and four anatomical landmarks identified on the mesh, namely the nasion (Nz; the point between the forehead and the nose), the inion (Iz; the most prominent point of the external occipital protuberance), and the left and right preauricular points (LPA and RPA; depressions located just anterior to the tragus of each ear). Using these landmarks, the algorithm defines reference planes, calculates geodesic paths on the head surface, and determines electrode coordinates according to standard proportional distances. All computations were implemented in MATLAB R2025a [10]. All vertices of the head mesh and the anatomical landmarks are represented as position coordinates in a common three-dimensional coordinate system in the form of (x, y, z). Nz, Iz, LPA, and RPA are therefore defined as reference points within the same 3D coordinate system. Direction vectors are computed from the differences between landmark coordinates (e.g., Iz − Nz), and the normal vectors of planes are obtained from the cross-products of these direction vectors. Based on these vector operations, all reference planes and geometric relationships used in the subsequent procedures are defined. Below, we describe the procedure in detail for (1) the standard 10–20 and 10–10 system coordinates, (2) the extended occipital (cerebellar) coordinates, and (3) the extended facial coordinates. Fig. 1 presents a flowchart summarizing the overall procedure of the proposed EEG electrode localization algorithm.

Standard EEG Coordinate Calculation (10–20 and 10–10 System): Fig. 3 illustrates the overall procedure for computing the international 10–20/10–10 system electrode positions on the 3D head mesh. First, two orthogonal reference planes are established using the anatomical landmarks.

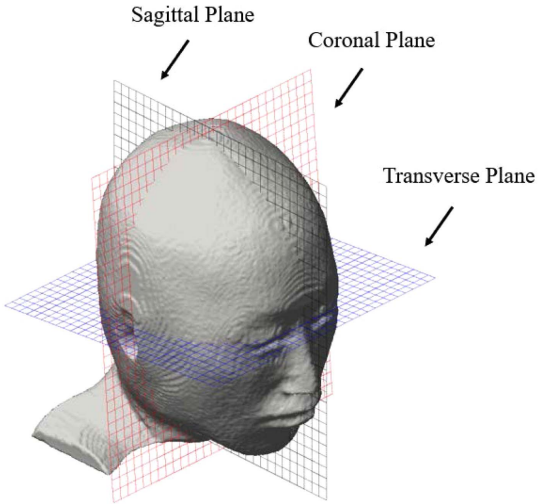

Fig. 2. (Color online) Three orthogonal anatomical reference planes (sagittal, coronal, and transverse) constructed on the 3D head mesh.

Figure 2 illustrates the three orthogonal anatomical reference planes (sagittal, coronal, and transverse) constructed on the 3D head mesh for defining the geometric framework of the proposed algorithm. The sagittal plane is defined by the points Nz and Iz and the head's vertical axis. This plane passes through the midline of the head, separating the left and right halves. Next, the coronal plane is defined through the Cz and LPA, RPA obtained from the sagittal plane. This plane separates the anterior and posterior sides of the head. The transverse plane (axis plane) is defined by using the points determined through the sagittal plane and the coronal plane. In fact, the transverse plane can be determined by positioning the horizontal plane with the direction vector using the coordinates of the frontal and occipital points (Fpz) of the medial sagittal plane and the coordinates of the temporal points (T7, T8) of the medial sagittal plane.

The normal vectors of these planes are obtained via cross-products of the defining vectors, ensuring that the planes are correctly oriented with respect to the head axes. The plane equation was employed as follow:

$$A_n x + B_n y + C_n z + D = 0 \quad (1)$$

Where A_n, B_n, and C_n represent the components of the normal vector to the plane, and D denotes the intercept of the plane.

Once the reference planes are set, their intersections with the 3D head mesh are computed to generate geodesic paths along the head surface. In particular, the intersection of the sagittal plane with the mesh yields the midline curve running over the top of the head from Nz to Iz. Along this midline path, the algorithm finds the point at 50% of the total geodesic distance from Nz to Iz and designates it as the vertex Cz (the midpoint, corresponding to the standard Cz electrode). Using the total Nz–Iz path length $L_{\mathrm{Nz–Iz}}$, the locations of other midline electrodes (e.g., Fpz, Fz, Pz, Oz) are determined at the appropriate percentages of this length according to the 10–20/10–10 system proportions. For example, Fpz and Oz are placed at 10% of the Nz–Iz distance from the nasion and inion, respectively, and so on, following standard EEG conventions. An analogous process is repeated for lateral paths: the head circumference and other great-circle paths (defined by the transverse plane and perhaps additional intermediate planes) are divided according to 10–10 ratios to locate lateral electrodes (such as T7/T8, F7/F8, etc.). The algorithm employs a shortest-path search on the mesh surface [11] to find optimal geodesic paths between reference points on these planes. The result of this

procedure is that all required geodesic paths for the 10–20 and 10–10 grids are identified, and the electrode coordinates at the standard 10% or 20% proportional intervals along each path are calculated. For example, the total geodesic path length L_{total} between Nz and Iz was calculated using the following equation:

$$L_{total} = \sum_{i=1}^{K-1} \sqrt{(x_{i+1} - x_i)^2 + (y_{i+1} - y_i)^2 + (z_{i+1} - z_i)^2} \quad (2)$$

Here, L_{total} represents the sum of the lengths of all segments that compose the entire path from Nz to Iz. K denotes the total number of vertices along the path, and x_i, y_i, z_i are the three-dimensional coordinates of the i-th vertex.

$$D = ratio \times L_{total} \quad (3)$$

Here, D indicates the cumulative geodesic distance from Nz to the target electrode position.

The variable ratio represents the proportional value defined by the international standard EEG system, and L_{total} denotes the total geodesic path length between Nz and Iz.

By iteratively applying these two steps: (A) computing a geodesic path between key landmarks, and (B) placing electrodes at fixed fractional distances along the path. The algorithm automatically computes the coordinates of all electrodes in the 10–20 and 10–10 systems on the given head model. Fig. 3 (a–i) summarizes these steps in sequence.

2.1. Extended Occipital (Cerebellar) Electrode Placement

To extend electrode coverage to the lower rear of the head (for targeting the cerebellum and brainstem regions), we introduced additional reference points and followed a systematic procedure to place a grid of electrodes below the standard occipital area. Fig. 4 illustrates this process.

First, starting from the inion (Iz), we define two new midline reference points further down the back of the head: one at 10% of the Nz–Iz distance below Iz and another at 20% below Iz. We denote these points as CBz (for “cerebellum zero”) and BSz (for “brainstem zero”), respectively (Fig. 4a). These serve as central anchor points for two new horizontal bands of electrodes in the extended occipital region. Next, a vertical geodesic path is drawn on the mesh from Iz down to BSz (Fig. 4b), representing the midline trajectory along which the new

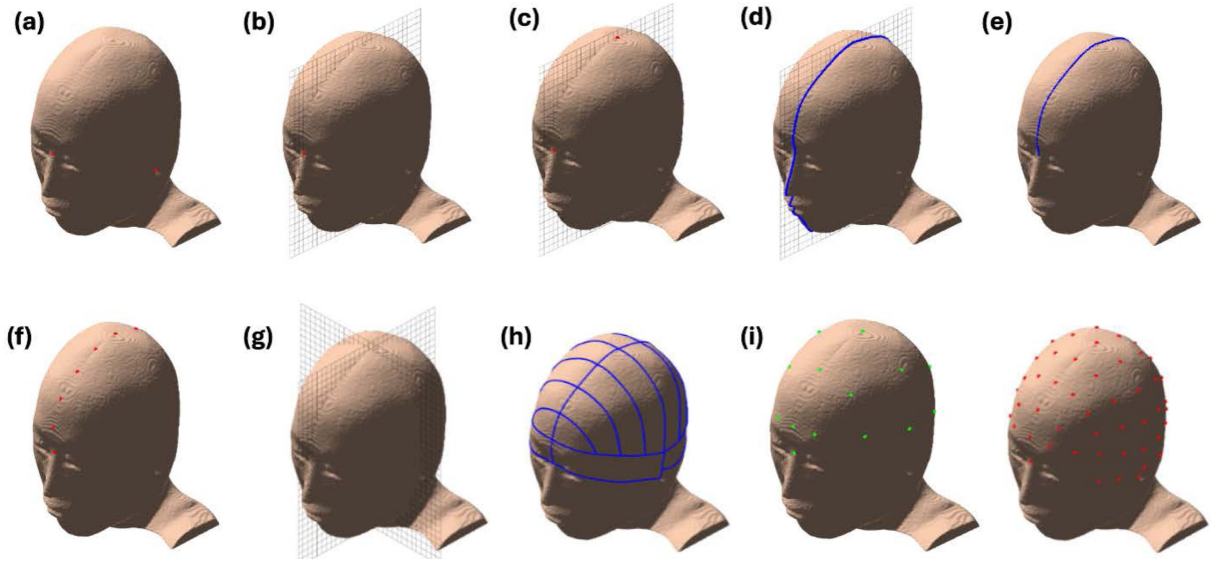

Fig. 3. (Color online) Overall procedure for computing the standard 10–20 and 10–10 EEG electrode coordinates on a 3D head surface mesh. (a) The algorithm begins with a 3D head mesh and four fiducial landmarks (Nz, Iz, LPA, RPA) identified by the user. (b) A plane passing through the nasion (Nz) and inion (Iz) is defined (sagittal plane) and used to intersect the head mesh. (c) The geodesic path along the mesh from Nz to Iz is computed, and the point at 50% of this path length is identified as Cz (vertex). (d) Additional intersection points along the Nz–Iz plane are found at specified proportions of the path. (e) A continuous midline path through these intersection points (from Nz to Iz) is obtained. (f) Electrode positions at the standard 10–20 and 10–10 proportional distances are calculated along each relevant path. (g) Using the previously computed points, new reference points are identified to define a perpendicular plane, and the process is repeated for that plane. (h) All the geodesic paths required to calculate the 10–20 and 10–10 positions are thus obtained. (i) In this manner, the coordinates of all electrodes in the 10–20 and 10–10 systems can be automatically computed by the algorithm.

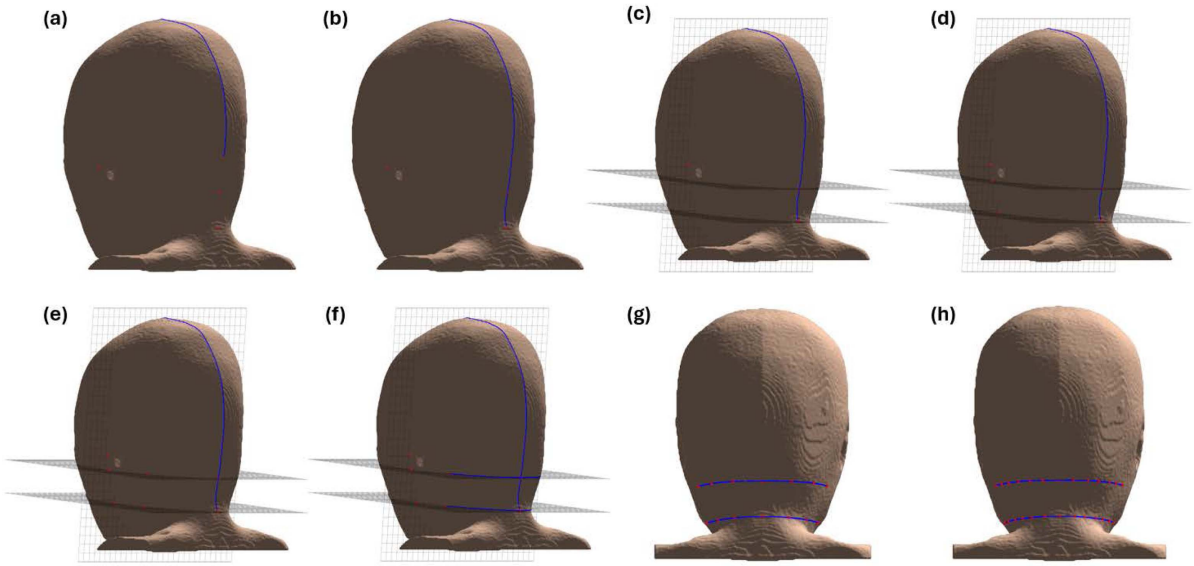

Fig. 4. (Color online) Procedure for extending electrode placement to the lower occipital (cerebellar) region. (a) Define central reference points CBz and BSz on the midline, located 10% and 20% of the Nz–Iz distance below the inion (Iz), respectively. (b) Draw a vertical path along the midline from Iz down to BSz. (c) At each center. point (CBZ, BSz), two horizontal reference planes and the LPA–Cz–RPA plane are defined. (d) Find the point where the LPA–Cz–RPA plane intersects the two horizontal planes. (e) Find 30% points each in the path to the intersecting point at CBz and the path to the intersecting point at BSz. (f) Compute the intersections of these planes with the 3D head mesh, yielding the curved paths connecting CB5–CB6 and BS5–BS6 around the back of the head. (g) Determine the positions of additional electrodes along each curved path (on both left and right sides), labeled CB1–CB4 on the upper (cerebellar) band and BS1–BS4 on the lower band, at specified proportional distances (e.g., 10% increments). (h) Using this approach, electrode positions can be calculated for an extended occipital grid (including finer 5% subdivisions) beyond the standard EEG coverage.

bands lie.

To determine the lateral boundaries of these bands dynamically, we utilize the coronal plane defined by the Left Preauricular Point (LPA), Vertex (Cz), and Right Preauricular Point (RPA). At each of the central levels (CBz and BSz), we define a horizontal plane and identify its intersection points with the LPA–Cz–RPA coronal plane (Fig. 4c–d). These intersections serve as the maximum lateral reference markers. We then trace the geodesic paths from the midline anchors (CBz and BSz) toward these lateral intersection points. To ensure the electrodes are focused on the posterior cerebellar region without extending too far laterally, we restrict the active path length to 30% of the distance from the midline to the intersection point (Fig. 4e).

Finally, curved surface paths are generated along the occipital scalp connecting the midline to these 30% boundary points (Fig. 4f). Along these defined curves, the electrode grid is distributed at equal intervals. This results in a set of new electrodes labeled CB1–CB4 along the upper (cerebellar) band and BS1–BS4 along the lower (brainstem) band. The numbering is chosen such that odd numbers indicate left-side electrodes and even numbers indicate right-side electrodes. The result of this procedure

Table 1. Summary of extended occipital (cerebellar and brainstem) electrodes.

Electrode	Relative Position
CBz	10% below Iz along the midline
CB1, CB3, CB5	Left lower occipital region, at successive 10% intervals from CBz
CB2, CB4, CB6	Right lower occipital region, at successive 10% intervals from CBz
BSz	20% below Iz along the midline
BS1, BS3, BS5	Left lower occipital region, at successive 10% intervals from BSz
BS2, BS4, BS6	Right lower occipital region, at successive 10% intervals from BSz
CB7–CB12, BS7–BS12	Additional electrodes at 5% subdivisions of the occipital geodesic paths

is an extended set of occipital electrodes covering the cerebellar region in a systematic way, adapted to the individual head shape using the coronal plane as a reference. (For nomenclature, the prefix "CB" indicates the upper occipital band near the cerebellum and "BS" the lower band near the brainstem; this naming convention was adopted with reference to previous suggestions in the literature.)

A concise summary of the extended occipital electrodes introduced by the proposed method is provided in Table 1.

2.2. Facial Electrode Placement

The algorithm also adds electrodes to the facial region by systematically extending the coordinate system from the nasion down to the chin. Fig. 5 shows the process for facial electrode placement. First, a midline reference line is established from the nasion (Nz) to the tip of the chin on the 3D head model (Fig. 5a). Along this line, we consider the 3D distance between Nz and the chin point and divide it into four equal segments. This yields three intermediate points (at 25%, 50%, 75% of the Nz–chin distance) which define three horizontal cross-sectional planes across the face. These planes correspond, in order, to approximate facial levels we label as N (nasion level, just below the nose bridge), T (nose Tip level), and M (Mouth level). Next, for each of these horizontal levels, we identify its intersection with a principal coronal path that runs around the head from the left preauricular point (LPA), over the vertex (Cz), to the right preauricular point (RPA) (Fig. 5b). The intersection points of each facial plane with the LPA–Cz–RPA path serve as lateral reference points for that plane. In essence, for each of the three face planes we have a central midline point (on the Nz–chin line) and a left and right reference point (where the plane meets the sides of the head near the ears or temple region). We then split each horizontal facial path at the midline: each plane's intersection curve on the face is divided into a left half and a right half, from the center point out to the side reference point. The algorithm computes the geodesic curve along the face for each half-section (Fig. 5c–d). Along each of these half-curve paths, we select three equally spaced points (corresponding again to 25%, 50%, 75% of the half-curve length). These points are assigned as the facial electrode positions. They are named as a series FA (for "facial") with a suffix indicating the level: FAN, FAT, and FAM correspond to the electrodes near the Nasion level, nose Tip level, and Mouth level, respectively. For each level, two electrodes are placed (one left, one right), and they are numbered with odd numbers for the left side and even numbers for

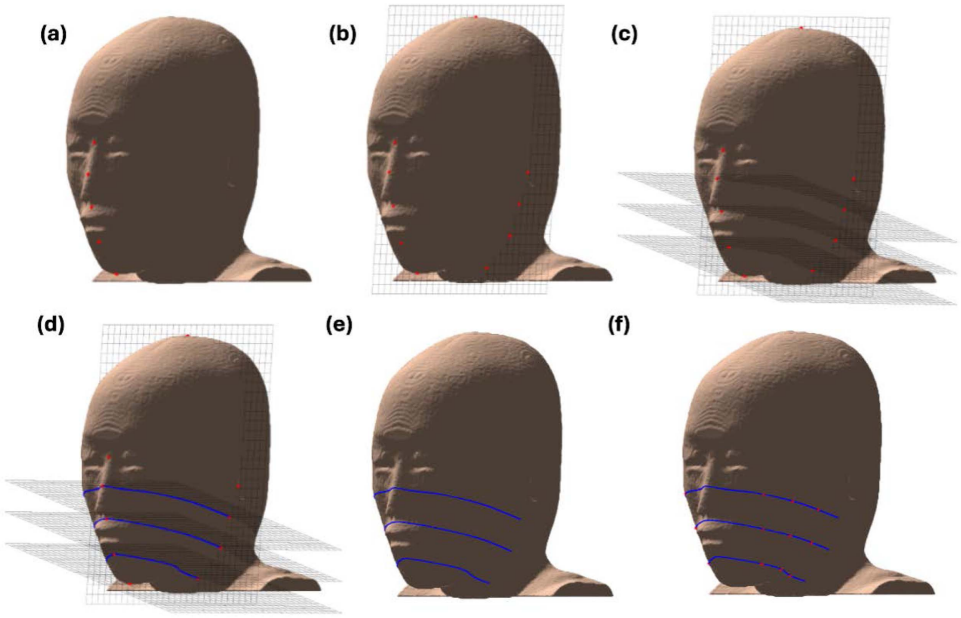

Fig. 5. (Color online) Facial electrode placement process. (a) Define the facial midline by the nasion (Nz) and the chin point, and set a facial center line along the profile. (b) Identify reference points where this facial midline's horizontal levels intersect the LPA–Cz–RPA plane (over the top of the head through the ears). (c) Create horizontal planes at the defined facial levels (N, T, M) passing through the respective reference points. (d) Compute the intersection of each plane with the 3D head mesh to produce curved paths on the face. (e) Remove the planes, leaving only the curved surface paths along the face. (f) Place electrodes along each curved path at the predetermined positions. These electrodes are labeled as the "FA" series (FAN, FAT, FAM), covering the facial regions from the nasion down to the chin.

Table 2. Summary of extended facial electrodes based on relative position.

Electrode	Relative Position
FAN1, FAN3, FAN5	25% down the Nz–chin line (N level), left side
FAN2, FAN4, FAN6	25% down the Nz–chin line (N level), right side
FAT1, FAT3, FAT5	50% down the Nz–chin line (T level), left side
FAT2, FAT4, FAT6	50% down the Nz–chin line (T level), right side
FAM1, FAM3, FAM5	75% down the Nz–chin line (M level), left side
FAM2, FAM4, FAM6	75% down the Nz–chin line (M level), right side

the right side (for example, FAN1 on the left and FAN2 on the right at the facial-nasion level, FAT1 and FAT2 at the tip-of-nose level, etc.). This scheme results in a structured grid of facial electrodes covering the forehead, cheeks, and perioral region in a symmetric fashion. Figure 5e–f illustrates the final curved paths on the face after removing the guiding planes, with electrodes positioned along each path. The extended facial electrode system systematically fills areas that are not included in the traditional EEG scheme, while maintaining consistent relative spacing.

A concise summary of the facial electrodes introduced by the proposed method is provided in Table 2.

3. Results

We applied the above algorithm to a 3D average head model (adult, ages 20–24) to compute the complete set of standard and extended electrode coordinates [12]. The algorithm successfully generated the positions of all traditional 10–20 and 10–10 system electrodes, as well as the additional electrodes in the occipital (cerebellar) and facial regions. All electrode coordinates were automatically mapped onto the 3D head mesh and then visualized for inspection. Every electrode was found to lie precisely on the head surface, following the local curvature of the scalp or face, which confirms the geometric accuracy of the placement.

Figure 6 presents the resulting electrode configurations from several viewpoints. Panel (A) shows the electrodes of the standard 10–10 system, and panel (B) shows those of the standard 10–20 system. These are visualized from multiple angles (Front, Left, Back, Right, Top) to verify that the positions align correctly on the head surface in all directions. It can be seen that the algorithm's outputs match the expected 10–20/10–10 locations and are smoothly distributed along the head according to the defined proportions. Panel (C) of Fig. 6 focuses on the extended occipital electrodes (cerebellar placement), shown in a posterior view. The new electrodes added at 10% and 5% intervals below the standard occipital area (CBz/BSz and associated points) are clearly visible. These added electrodes provide coordinate coverage for targeting the cerebellum and brainstem; the placement suggests that the algorithm can furnish the necessary positions for studies requiring stimulation of these deep regions. Panel (D) of Fig. 6 illustrates the facial electrode placements. The facial electrodes (FAN, FAT, FAM series) are shown covering the forehead, cheek, and chin areas that are not included in the conventional EEG system. They are systematically arranged along horizontal

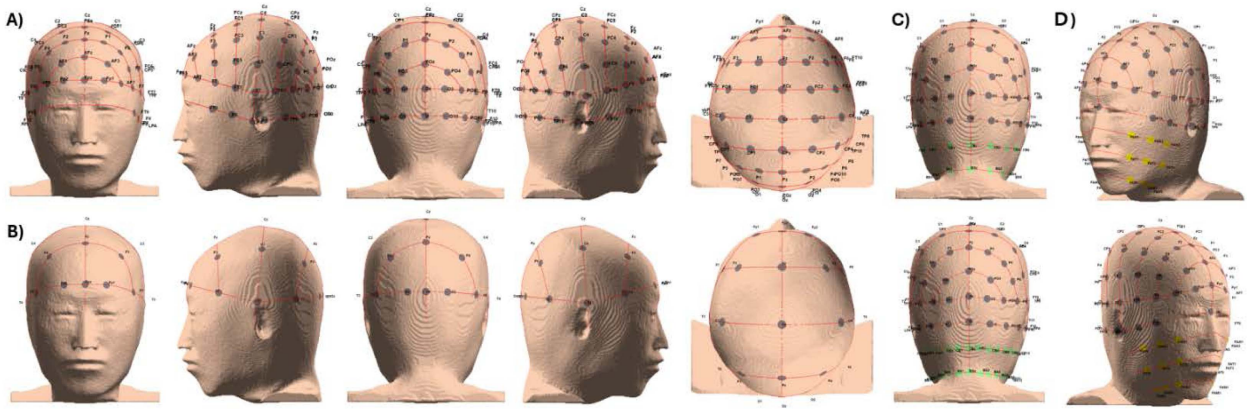

Fig. 6. (Color online) Visualization of the computed electrode layouts on the 3D head model, from various viewpoints. (Only the Back view is shown for the cerebellar extension, as it is not visible from other angles.) (A) Standard EEG 10–10 system electrode layout (full set of 76 electrodes). (B) Standard EEG 10–20 system layout (21 electrodes). (C) Extended cerebellar (occipital) electrode layout, showing the additional electrodes placed at 10% and 5% intervals below the standard occipital region (posterior view). (D) Extended facial electrode layout, showing the additional electrodes placed on the face (illustrated in an anterior/lateral view). All electrodes are correctly positioned on the head surface; in (A) and (B) they are shown from front/side/back/top perspectives to confirm alignment, while (C) and (D) highlight the new electrodes introduced by our algorithm.

bands defined by the nasion–chin framework, demonstrating that the algorithm successfully extended the electrode grid to the anterior aspect of the head. Fig. 6 includes only the back view for the occipital/cerebellar electrodes (since those are mainly posterior) and an appropriate view for the facial electrodes, while multiple perspectives are used for the standard systems for completeness.

To evaluate the algorithm's applicability to different head sizes and shapes, we further applied it to a set of age-specific average head models. We tested four head models representing ages 6 years, 9 years, 15 years, and 20–24 years (adult). These 3D head meshes were obtained from a public dataset of average head shapes for different age groups. The electrode placement algorithm was run on each model without any modification of parameters. Fig. 7 summarizes the results for these age groups. In all cases, the algorithm was able to compute and map the full set of 10–20, 10–10, facial, and cerebellar electrodes onto the head surface successfully. As expected, the absolute distances between electrodes vary with head size, but the relative spacing (in terms of percentage of head dimensions) is preserved by the algorithm. We observed that for the smaller head models (e.g., age 6), some of the visualized electrode markers appeared closer together or slightly overlapping in the rendering. This minor overlap is a visualization artifact due to using the same marker size for all heads; it indicates that on a very small head, the physical electrode discs might touch or overlap if not resized. Importantly, the algorithm's placement logic still held – the electrodes were positioned at the correct proportional locations even on the smallest head. This demonstrates that the method can be applied to subjects of different ages (and by extension, different head sizes), with the electrode coordinates scaling appropriately to the individual's head geometry. The systematic nature of the placement is maintained across all models. The results for each age group are shown in Fig. 7, confirming that the extended electrode montage can be reproduced on a variety of head shapes.

The electrode placement algorithm developed in the course of this study was cross-validated by comparing it

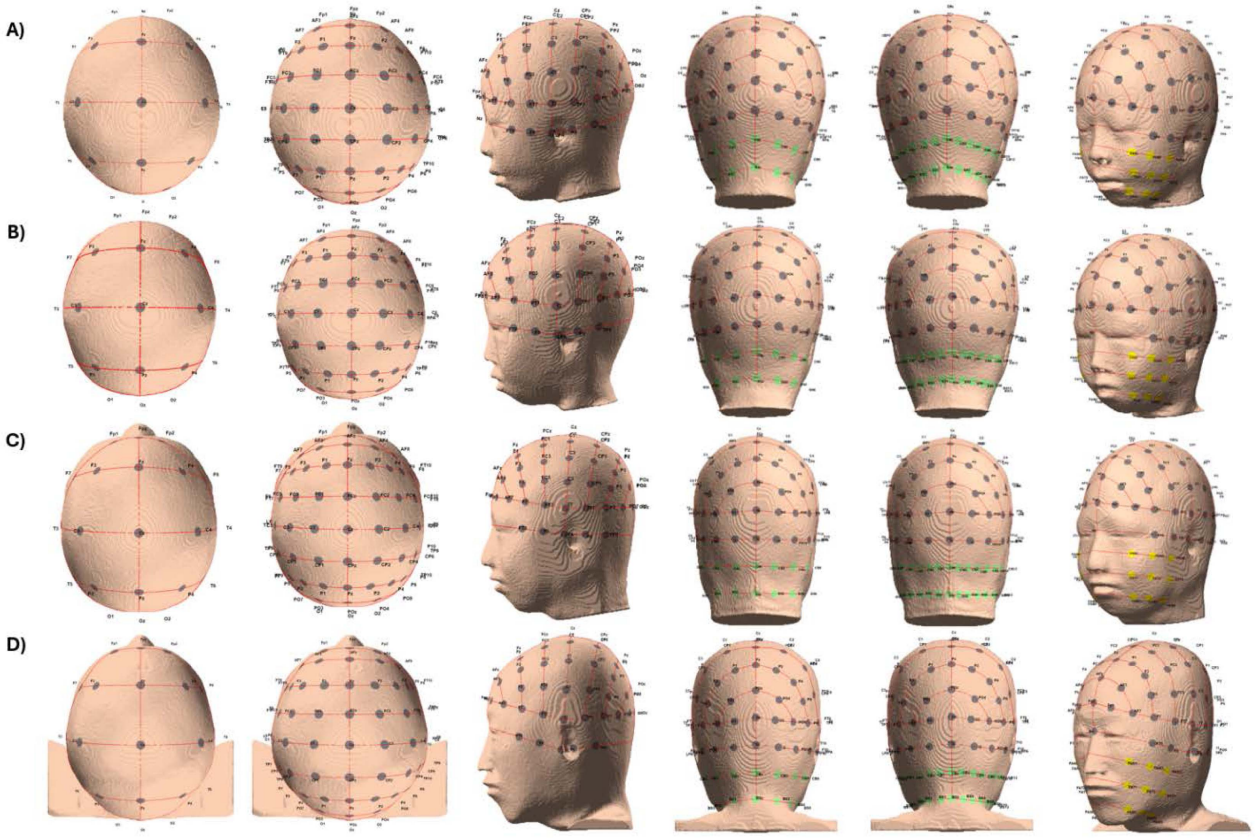

Fig. 7. (Color online) Electrode placement results on head models of different ages, using the standard 10–20 and 10–10 systems plus the extended occipital and facial electrodes. (A) Average head model for age 6 years. (B) 9-year-old average head model. (C) 15-year-old average head model. (D) 20–24 years (young adult) average head model. The algorithm automatically adjusts the electrode spacing to each head's size, successfully placing all electrodes in the correct proportional locations for each age group.

with conventional EEG position induction algorithms. For comparison, we compared T1-MRI images from random people (IXI100-Guys-0747-T1, IXI127-H-1451-T1, IXI167-H-1569-T1, IXI167-H-1642-T1, IXI244-H-0841-T1, IXI443-H-2215-T1, IXI477-IOP-115-T1, IXI561-IOP-115-T1, IXI561-IOP-115-T1, IXI561-IOP-1152-T1) based on the functionality of SimNIBS, which provides tissue segmentation and EEG coordinates to open sources [13, 14]. Among the EEG coordinates provided by SimNIBS, 10–10 system algorithms of Cutini *et al.* (2011), Neuroelectrics, Jurcak *et al.* (2007) were used [4, 15, 16]. First, in the 10–10 system verification, three existing algorithms and the electrode placement results of the proposed algorithm are shown in 10 models. It also shows the center point so that the center point of the three existing algorithms can be compared with the center point of the proposed algorithm. The results of the electrode placement between algorithms are shown in Fig. 8. To show these results in detail, illustrations from various angles are presented in Fig. 9.

Table 3 shows the results of comparing the center point of the results of the three algorithms derived in the SimNIBS charm-based division for each model, the average distance and standard deviation of the existing algorithm and the proposed algorithm. The analysis showed that the mean placement error of our proposed algorithm falls within the variability range of the existing algorithms. For the ten models tested, the existing algorithms have an average deviation of ~2.66 ± 2.18 (mm) while our algorithm shows an average deviation of ~3.41 ± 2.03 (mm). This suggests that our algorithm's accuracy is comparable to the conventional methods, as its error is within the existing methods' error range. This means that the two algorithms show a similar level of

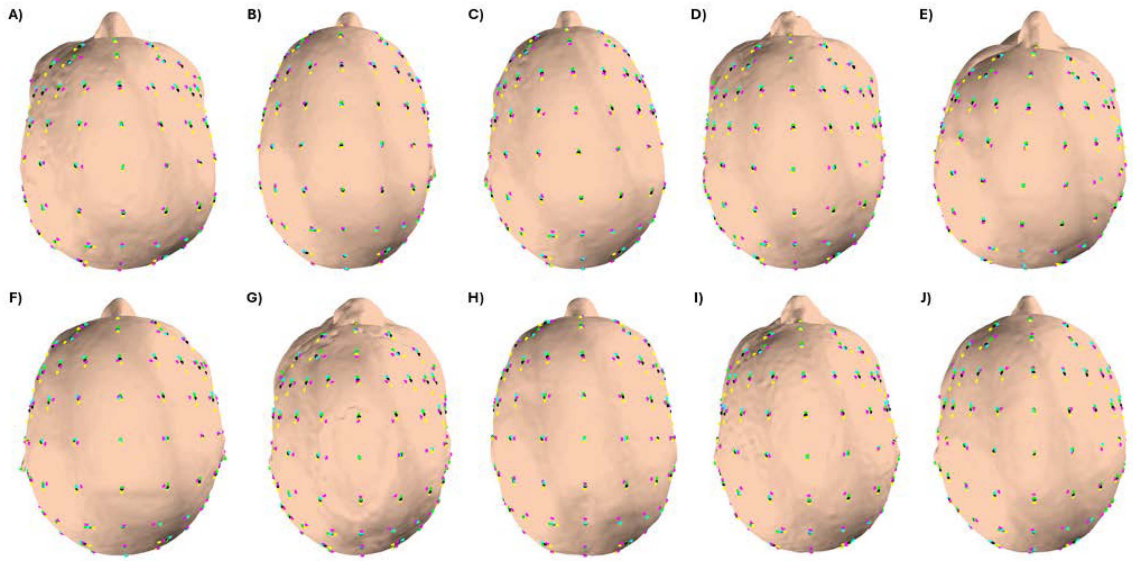

Fig. 8. (Color online) The verification results of algorithms from Model 1 to Model 10. (Magenta color is our algorithm and black is the center point of the three existing algorithms. The remaining Cutini2011 (blue), Neuroelectrics (yellow), and Jurcak 2007 (green) are the electrode coordinates for each of the other three algorithms.)

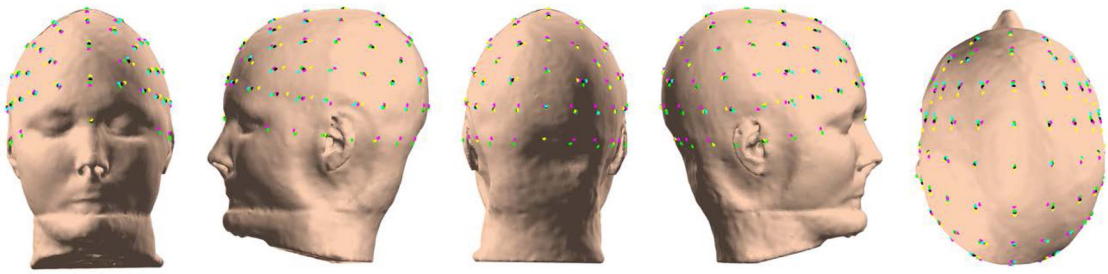

Fig. 9. (Color online) Algorithm validation results for Model 10. Results between algorithms are visualized from multiple angles (front, left, back, right, top) to confirm electrode placement.

Table 3. Average distance and standard deviation for each model of 10-10 System (Unit: mm).

Models	Existing algorithms	Proposed (10-10)
Model 1	2.77 ± 2.25	3.86 ± 2.24
Model 2	2.67 ± 2.19	3.27 ± 1.88
Model 3	2.83 ± 2.35	3.36 ± 1.97
Model 4	2.62 ± 2.15	2.81 ± 1.75
Model 5	2.50 ± 2.04	3.45 ± 2.35
Model 6	2.61 ± 2.11	3.34 ± 2.04
Model 7	2.70 ± 2.24	3.73 ± 1.91
Model 8	2.64 ± 2.17	3.77 ± 2.40
Model 9	2.72 ± 2.21	3.26 ± 1.81
Model 10	2.55 ± 2.05	3.26 ± 1.91

position estimation performance and that the proposed algorithm derives a similar electrode position when compared to the existing method. The fact that the average distance of the proposed algorithm exists within the error range of the existing algorithm shows that the proposed algorithm maintains the overall stability and consistency. The average distance and standard deviation for each model are presented in Table 3 below.

In the 10–20 system verification, the three center points of the existing algorithms used in the 10–10 system and the electrode placement results of the proposed 10–20 system algorithm are shown in 10 models. The results of the electrode placement between algorithms are shown in Fig. 10. To show these results in detail, illustrations from various angles are presented in Fig. 11.

Table 4 shows the results of comparing the mean distance and standard deviation of the three existing algorithms used in the 10–10 system with the average distance of the proposed algorithm. On average across the ten models, the distance between our algorithm's electrode positions (for the extended 10–20 system) and the three

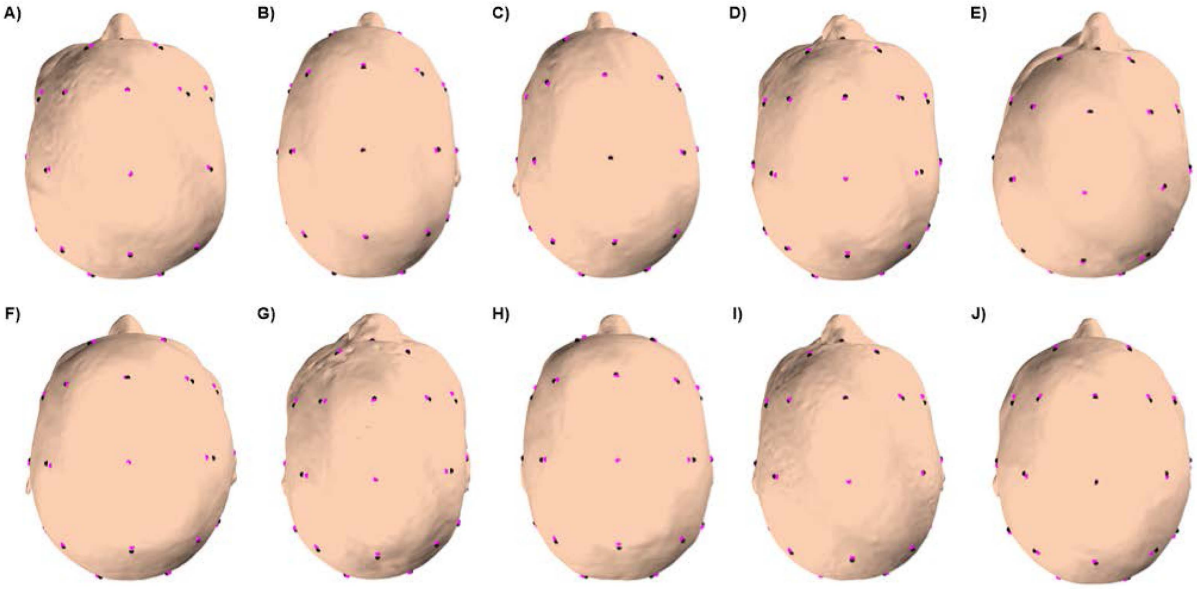

Fig. 10. (Color online) Compare three existing algorithms (Cutini 2011, Neuroelectrics, and Jurcak 2007) in the 10–10 system with the proposed 10–20 system algorithm (Cutini 2011, proposed algorithm: magenta).

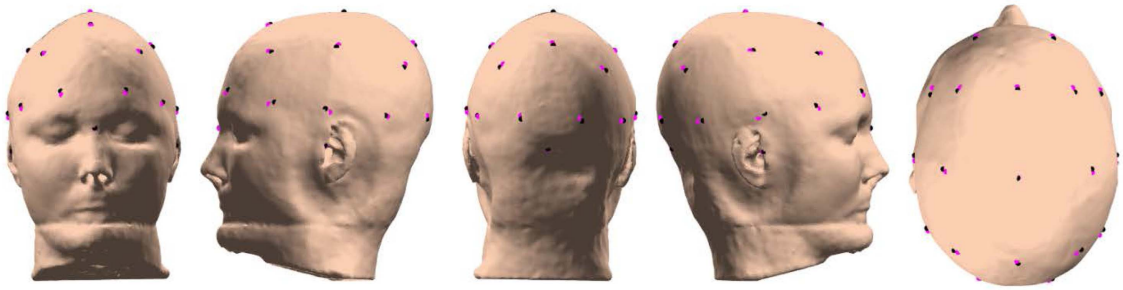

Fig. 11. (Color online) Algorithm validation results for Model 10 (extended 10–20 system). The differences between algorithms are shown from multiple angles (front, left, back, right, top) to confirm electrode placement.

Table 4. Average distance and standard deviation for each model of 10–20 System (Unit: mm).

Models	Proposed (10-20)
Model 1	3.43 ± 2.79
Model 2	2.55 ± 1.88
Model 3	2.33 ± 1.37
Model 4	3.07 ± 1.76
Model 5	2.47 ± 1.83
Model 6	2.80 ± 1.98
Model 7	3.29 ± 2.40
Model 8	3.59 ± 2.56
Model 9	2.39 ± 1.62
Model 10	3.17 ± 1.76

algorithms' combined reference center point was about 2.91 ± 2.00 (mm), indicating the typical placement difference. The mean distance and standard deviation of each model are presented in Table 4 below.

Comparison with the method verified by SimNIBS in this study shows that SimNIBS has a tolerance range of 3 mm to 1cm [17]. Since the mean distance and standard deviation of the proposed algorithm are about 3 to 5 mm, it is included within the tolerance range based on SimNIBS. Therefore, the proposed algorithm is judged to have secured the reliability of SimNIBS level in calculating the personalized electrode position.

4. Discussion

In this study, we successfully developed an automated electrode localization algorithm that, using a 3D head model and a few anatomical landmarks, extends the standard EEG coordinate system to include facial and lower occipital regions. The proposed methodology overcomes spatial limitations of the conventional EEG placement systems and has several important implications for advancing precision in brain stimulation technologies.

First, our algorithm addresses the issues of reproducibility and accuracy in electrode placement. Traditional manual measurement (using EEG caps or tape measures) is prone to substantial inter-operator error and cannot easily account for individual variations in head shape. In contrast, the algorithm uses only minimal landmarks (Nz, Iz, LPA, RPA) and automatically calculates personalized 3D coordinates for all electrodes, enabling consistent and reproducible placement across different operators and subjects. This consistency can greatly improve the reliability of non-invasive brain stimulation (NIBS) experiments, especially for techniques like tDCS, tACS, and multi-channel TIS that are highly sensitive to electrode positioning. By ensuring that electrodes are placed in the intended locations for each individual, the algorithm enhances experimental rigor and comparability.

Second, the extension of the coordinate system to facial and cerebellar regions supports new neuromodulation paradigms targeting deep or lower brain structures. There is a growing interest in stimulation studies focusing on regions such as the hippocampus, brainstem, and cerebellum. These require electrodes to be placed on unconventional locations like the cheek, the nasal bridge area, or the lower back of the head. Previously, the lack of a standardized coordinate system for these areas made it difficult to design experiments and to compare results across studies. Our work provides the first systematic framework for electrode placement in these regions, by introducing a Nasion–chin based facial grid and an Iz-based occipital extension. This framework is novel and helps fill the gap noted in prior literature that asked whether and how EEG coordinates could be established for the cerebellum or face. With this extended system, future studies involving facial electrodes (e.g. for TIS targeting the hippocampus) or cerebellar tDCS can follow a standardized set of placement guidelines, improving cross-study consistency and reducing setup guesswork.

Third, the integration of visualization in our algorithm improves its practical utility in clinical and research settings. The algorithm outputs a 3D electrode map that allows researchers or clinicians to intuitively inspect electrode positions on a virtual head before actual placement. This visual feedback makes it easier to verify that the intended targets (from computational models or MRI-based planning) correspond to the real electrode locations, and to adjust if necessary. In complex multi-electrode montages, the ability to see all electrode positions in 3D helps to minimize spatial errors (such as electrodes placed too close together or misaligned) and thereby contributes to the accuracy of the stimulation. The improved confidence and clarity in electrode positioning can facilitate the translation of advanced multichannel stimulation protocols to practical use.

Fourth, the proposed algorithm holds significant clinical implications for optimizing current distribution in non-invasive brain stimulation (NIBS) applications such as tDCS, tACS, and TIS. In previous tDCS or tACS studies targeting the cerebellum, reference electrodes had to be placed on the chin, cheek, or lower occiput to control current flow. However, the standard 10–20 and 10–10 systems do not include these regions, making standardized placement difficult and often relying on the subjective experience of the clinician. This study resolves this issue by providing systematic coordinates for the facial and

lower occipital regions.

Furthermore, for Temporal Interference Stimulation (TIS)—a relatively recent NIBS technique for stimulating deep brain structures—the interference waveform resulting from the intersection of electric fields of different frequencies is key to stimulation. Therefore, the configuration of stimulation parameters, such as electrode placement, is directly linked to the targeting accuracy for the region of interest (ROI). By utilizing the extended electrode placement, which includes the face and lower occiput via our algorithm, the TIS stimulation patterns can be regulated more precisely. This not only enables stimulation of a broader range of brain areas that were previously difficult to access with conventional electrode placement methods but also allows for the design of more focal and diverse stimulation protocols for deep brain targets.

Despite its strengths, our approach has some limitations. The accuracy of the algorithm is dependent on the correct identification of the initial fiducial landmarks on the head. If a landmark like the nasion or preauricular point is marked incorrectly on the 3D model, that error will propagate through the coordinate calculations and could offset multiple electrode positions. In future work, this limitation could be mitigated by incorporating automatic landmark detection techniques (for example, using 3D image processing or machine learning on facial geometry) to reduce user dependence and potential errors. Achieving fully automatic landmark identification would allow the entire electrode placement process to be automated end-to-end. Another consideration is that our current algorithm bases electrode coordinates on fixed anatomical proportions derived from the standard EEG system. While this is a logical approach, it does not account for population variability beyond those proportions. Future research could leverage large databases of head shapes across different ages, genders, and ethnic groups to refine the coordinate system statistically. By building an extensive normative model (for instance, using principal component analysis of head shape variations), one could adjust the electrode locations to better fit specific sub-populations or to optimize targeting of certain brain regions. Such extensions would further enhance the generalizability and precision of the electrode placement framework. Proposed algorithm divides the head coverage similar to SimNIBS but with a different approach: SimNIBS uses a projection-based method, whereas we use plane-intersection geometry. Because of this difference, we observed slightly larger positioning errors at certain central electrode points when comparing our results to those of the three existing algorithms. Typically, EEG coordinate algorithms are validated on data from 20+ individual subjects. However, due to practical constraints, we could not perform a large-scale validation with human subjects in this study.

When deploying the temporal electrodes of the 10-10 system, the proposed algorithm calculates the path along the surface of the head model through the plane equation and places the electrodes at a constant rate, and there is room for the mesh model used in this study to enter the ears. Therefore, it can be seen that the electrodes behind the LPA and RPA have paths that are created and gathered along the space of the ears. When actually deploying the electrodes through the algorithm, it is necessary to place the electrodes with these considerations in mind. We noticed that for the 10–10 system, the algorithm's geodesic path runs close to the ear region, causing the electrodes just behind LPA/RPA to cluster near the ears. Thus, when using the algorithm, one should be mindful of this and adjust any electrodes that fall around the ears to ensure proper placement

5. Conclusion

We successfully developed fully automated software for EEG electrode localization on a 3D head model that extends the conventional 10–10 system to the face, lower occiput, and cerebellar regions. The software computes a complete, individualized set of electrode coordinates with high precision and excellent reproducibility. By providing a standardized template for placements over previously unsupported facial and inferior posterior areas, it enables accurate targeting of deep brain structures and the cerebellum. This capability is particularly advantageous for TIS, where precise multi-source alignment is essential for focal delivery to deep targets. Beyond immediate applications to tDCS, tACS, TIS, and other neuromodulation techniques, the automation and standardization built into our pipeline make high-throughput, large-scale ("big-data") studies readily achievable, reducing operator burden and facilitating seamless data aggregation across participants and sites. We anticipate that this software will underpin more consistent, precise, and efficient EEG-guided stimulation protocols and accelerate both research and clinical translation.

Acknowledgement

This research was supported by the Bio&Medical Technology Development Program of the National Research Foundation (NRF) funded by the Korean government (MSIT) (No. RS-2024-00356694). This result was supported by the "Regional Innovation System &

Education (RISE)" through the Gwangju RISE Center, funded by the Ministry of Education (MOE) and the Gwangju Metropolitan Government, Republic of Korea (2025-RISE-05-011).

References

[1] A. J. Woods, A. Antal, M. Bikson, P. S. Boggio, A. R. Brunoni, P. Celnik, L. G. Cohen, F. Fregni, C. S. Herrmann, E. S. Kappenman, H. Knotkova, D. Liebetanz, C. Miniussi, P. C. Miranda, M. A. Nitsche, W. Paulus, A. Priori, D. Reato, C. Stagg, and N. Wenderoth, Clin. Neurophysiol. **127**, 1031 (2016).

[2] T. G. Kim, N. Y. Seo, Y. J. Jung, and J. W. Park, J. Magn. **29**, 467 (2024).

[3] N. Grossman, D. Bono, N. Dedic, S. B. Kodandaramaiah, A. Rudenko, H.-J. Suk, A. M. Cassarà, E. Neufeld, N. Kuster, L.-H. Tsai, A. Pascual-Leone, and E. S. Boyden, Cell **169**, 1029 (2017).

[4] V. Jurcak, D. Tsuzuki, and I. Dan, NeuroImage **34**, 1600 (2007).

[5] P. Giacometti, K. L. Perdue, and S. G. Diamond, J. Neurosci. Methods **229**, 84 (2014).

[6] L. Koessler, L. Maillard, A. Benhadid, J.-P. Vignal, J. Felblinger, H. Vespignani, and M. Braun, NeuroImage **46**, 64 (2009).

[7] I. R. Violante, K. Alania, A. M. Cassarà, E. Neufeld, E. Acerbo, R. Carron, A. Williamson, D. L. Kurtin, E. Rhodes, A. Hampshire, N. Kuster, E. S. Boyden, A. Pascual-Leone, and N. Grossman, Nat. Neurosci. **26**, 1994 (2023).

[8] A. Liu, M. Vöröslakos, G. Kronberg, S. Henin, M. R. Krause, Y. Huang, A. Opitz, A. Mehta, C. C. Pack, B. Krekelberg, A. Berényi, L. C. Parra, L. Melloni, O. Devinsky, and G. Buzsáki, Nat. Commun. **9**, 5092 (2018).

[9] A. Opitz, A. Falchier, C.-G. Yan, E. M. Yeagle, G. S. Linn, P. Megevand, … and C. E. Schroeder, Sci. Rep. **6**, 31236 (2016).

[10] The MathWorks Inc., MATLAB, version R2025a. Natick, MA: The MathWorks Inc., 2025.

[11] G. Peyré and L. Cohen, Int. J. Comput. Vis. **69**, 145 (2006).

[12] Korea Electronics and Telecommunications Research Institute (ETRI), Human (average head) virtual model [Data set], ETRI Data Repository (2022).

[13] IXI Dataset, available at https://brain-development.org/ixi-dataset/ (accessed Sep. 22, 2025).

[14] O. Puonti, K. Van Leemput, G. B. Saturnino, H. R. Siebner, K. H. Madsen, and A. Thielscher, NeuroImage **219**, 117044 (2020).

[15] Neuroelectrics, “EEG device coordinate system,” https://www.neuroelectrics.com/eeg.

[16] S. Cutini, P. Scatturin, and M. Zorzi, NeuroImage **54**, 919 (2011).

[17] G. B. Saturnino, O. Puonti, J. D. Nielsen, D. Antonenko, K. H. Madsen, and A. Thielscher. EMBC (2019) pp. 3-25.